Assessment of geometrical defects caused by thermal distortions in laser-beam-melting additive manufacturing: a simulation approach

Corentin Douellou, Xavier Balandraud, Emmanuel Duc

Assessment of geometrical defects due to thermal distortions in laser-beam-melting additive manufacturing: a simulation approach

Corentin Douellou, Xavier Balandraud and Emmanuel Duc
Université Clermont Auvergne, CNRS, SIGMA Clermont, Institut Pascal, Clermont-Ferrand, France

Abstract

Purpose – The purpose of this paper is to develop a numerical approach inspired by Geometrical Product Specifications (GPS) standards for the assessment of geometrical defects appearing during Additive Manufacturing (AM) by Laser Beam Melting (LBM).

Design/methodology/approach – The study is based on finite element (FE) simulations of thermal distortions, then an assessment of flatness defects (warping induced by the high residual stresses appearing during the manufacturing) from the deformed surfaces provided by simulation, and finally the correction of the calculated flatness defects from preliminary comparison between simulated and experimental data.

Findings – For an elementary geometrical feature (a wall), it was possible to identify the variation in the flatness defect as a function of the dimensions. For a complex geometry exhibiting a significant flatness defect, it was possible to improve the geometric quality thanks to the numerical tool.

Research limitations/implications – This work is the first attempt using a numerical approach inspired by GPS standards to identify variations in thermal distortions caused by LBM, which is an initial step towards optimization. This paper is mainly focused on flatness defect assessment, even though the approach is potentially applicable for all types of geometrical defects (shape, orientation or position defects).

Practical implications – The study opens prospects for the optimization of complex parts elaborated using LBM, based on the minimization of the geometric defects caused by thermal distortions.

Social implications – The prospects in terms of shape optimization will extend the potential to benefit from the new possibilities offered by LBM additive manufacturing.

Originality/value – Unlike the usual approach, the proposed methodology does not require

any artifacts or comparison with the CAD model for geometrical distortion assessment. The present approach opens up the possibility of performing metrology from FE simulation results, which is particularly promising in the AM field.

Keywords Additive manufacturing, Geometrical specification, Thermal distortions, Process simulation, Laser beam melting, Powder bed fusion, Tolerancing, Flatness, Straigthness

Paper type Research paper

1. Introduction

Additive manufacturing (AM) offers new possibilities that change classic manufacturing processes and challenge the usual design approaches. Among the different AM techniques, laser beam melting (LBM) is of particular interest to cutting-edge industries (in particular aeronautics, space and defense) because it provides the possibility of manufacturing metallic parts with complex geometries. The technology is based on a “layer upon layer” manufacturing principle. For each layer, a laser beam is used as an energy source to heat and melt a metallic powder bed. LBM brings new perspectives but also new constraints, modifying all the usual approaches to design and manufacturing. It offers the possibility to produce parts with new geometries as well as complete mechanical systems (assemblies of mechanical parts) in a single manufacturing process. However, obtaining final products by LBM is not easy in many cases. Industrial requirements for metallic parts are in general severe in terms of material quality and geometric precision, while the optimization of process parameters is difficult to perform because of the numerous physical mechanisms involved. The process parameters influence the mechanical performances of the printed material such as fatigue endurance (Becker and Dimitrov, 2016; Santos *et al.*, 2016; Douellou *et al.*, 2019), but also impact the geometrical quality of the elaborated part because of thermal distortions. The present study focuses on the quantification of these distortions from simulations of the LBM manufacturing process, and on the implications in terms of manufacturing strategy choices for minimizing geometric errors.

Considering a mechanical part intended to be inserted into a mechanical system and additively

manufactured, the issue is to ensure the correct geometrical specifications inside the process, in order to avoid expensive post-processing. Within the process of producing a part, several stages may induce geometrical defects (Jared *et al.*, 2017; Hällgren *et al.*, 2016; Jin *et al.*, 2017; Umaras and Tsuzuki, 2017): STL file generation, slicing operations, layer filling and matter formation. In particular, thermal distortions occur during the manufacturing process due to strong temperature gradients and extreme cooling rates. The problem of designing a part for AM is raised. Several studies have explored the methodology of Design For Additive Manufacturing (DFAM) in order to address this problem. Two questions are considered in DFAM methodologies: how to position the functional surfaces in the machine to improve their quality and how to place the matter between these functional surfaces (Ponche *et al.*, 2014; Sossou *et al.*, 2017). The first question is related to the notion of geometrical specifications and tolerancing. Ponche *et al.* also mention in their study the use of process simulation as an entry point for DFAM tools. The second question, regarding the placement of matter between the surfaces, is mainly answered by topological optimization tools in the literature. As a first approach in the present work, we explored the idea of the parametric optimization of a part to be designed for LBM.

Once a part has been geometrically designed for AM, it should be considered for production on a given machine, which will generate deviations during the execution of the process. Two types of approach have been proposed in the literature:

- The first approach consists of studying the production of a specific part on this machine. More precisely, the question is to evaluate and control the geometrical deviations between the specified geometry and the distorted geometry obtained at the end of the manufacturing process. Many studies have dealt with process-related geometrical deviations. They are based on the measurement of the distances between points on the real surface and the nominal surface. In this case, the STL model is used as nominal part, and the deviations are evaluated on the vertices of the facets (Zhu *et al.*, 2017). Moroni *et al.* pointed out that Geometric Dimensioning and Tolerancing (GD&T) and Geometrical Product Specification (GPS) standards were designed to be used in a two-dimensional space. They proposed a specific voxel model to define and evaluate geometric deviations throughout the process (Moroni *et al.*, 2017);
- The second approach consists of manufacturing and measuring an artifact in order to assess the accuracy of the machine, focusing on the machine and the overall process and not on the AM part itself. Several types of parts have been proposed. Braian *et al.*

analyzed the precision of parts for dentistry from specific implant shapes (Braian *et al.*, 2016). Specific dimensions were measured and compared to nominal ones. However, the process for dentistry is not applicable to a general process, as there are no geometric tolerance specifications. Yap *et al.* proposed several shapes of part to evaluate the distortion of thin walls and small gaps (Yap *et al.*, 2017). The capability of the process was evaluated through the feasibility of the shape as a function of the dimensions. Lieneke *et al.* defined the tolerance interval class of an AM process by measuring linear dimensions in the machine space (Lieneke *et al.*, 2015; Lieneke *et al.*, 2016). Sharain proposed a global approach consisting of manufacturing and controlling an artifact with geometric specifications defined according to ISO 1101 (Shahrain *et al.*, 2016), for a rapid evaluation of the process.

One of the objectives of these approaches is to assess the capability of the process during industrialization and to relate it to ISO standards. Mashid *et al.* proposed a statistical analysis focused on this aspect (Mahshid *et al.*, 2017). Dantan *et al.* worked directly on the functional accuracy assessment of assemblies rather than the verification of geometric specifications (Dantan *et al.*, 2017; Huang *et al.*, 2018).

In this framework, the present paper aims to develop the idea of using simulation results as an entry point for geometrical defect evaluation, shape optimization through geometrical defect evaluation, and the assessment of the manufacturing capability of the process. Simulation results and experimental findings have been compared to assess simulation accuracy. The prospect of performing numerical metrology from finite element simulation results is really promising in the case of AM. Indeed, this opens up the possibility of integrating geometrical specifications in the part/assembly design, and evaluating the distortions of the functional surfaces rather than using an artifact or a comparison with the CAD model.

Several metals can be processed using LBM. Among these, Ti6Al4V titanium alloy offers good weldability. It is well known for its high strength, low weight resistance, very good corrosion resistance and bio-compatibility. It is one of the more common metals in AM because of its aeronautical and medical applications, and was chosen for the application cases in the present paper, which is organized as follows. Section 2 presents the numerical approach employed in the study, including experimental calibration performed in terms of flatness defect values. This type of defect is referring to the curvature of a surface initially designed to

be flat and that has been subjected to a warping during the manufacturing process. Section 3 is dedicated to the application to two geometric configurations, namely a wall (elementary "design block") and a complex geometry prone to large flatness defects. Remarks and a conclusion close the paper.

2. Numerical approach

The present study is based on a numerical procedure that was experimentally calibrated. Three points are developed in this section. First, Section 2.1 presents the simulation software that was employed to calculate thermal distortions accompanying the LBM process. Next, Section 2.2 explains the methodology to assess geometric defects from the deformed surfaces provided by the simulation software. Finally, Section 2.3 provides a comparison with experimental data in order to calibrate the numerical results.

2.1 Simulation tool

The numerical tool used in the study is ESI Additive Manufacturing 2018.0 (prototype version) provided by ESI Group (ESI Group, 2018). It is a finite element package in which elements are activated successively layer by layer from the building plate, similarly to the LBM process. It is possible to activate several layers at the same time for faster calculations, *i.e.* to consider finite elements whose height is a multiple of the real layer thickness (the term "superlayer" is used in (Peng *et al.*, 2018a; Peng *et al.*, 2018b)). More generally, different mesh strategies can be chosen, including an approach by strips rather than by whole layers or superlayers (see below for additional information about mesh choice). Thermal contraction strains due to cooling from solidus temperature to chamber temperature are applied to each created layer (Megahed *et al.*, 2016). Final strains in the created layer at chamber temperature are different from these applied thermal strains because of the appearance of elastic and plastic strains. The latter result from the presence of the already solidified layers, whose stiffness counteracts the thermal contraction of the new layer. As a consequence, the return to chamber temperature of a new layer also deforms all the layers below.

The building plate is considered as being made of the same material as the part to be

manufactured. It is assumed to be at chamber temperature during the manufacturing process. It is subjected to thermal distortions due to its anchorage with the part. The separation of the part from the building plate was not considered in the present study, although this option is proposed by the software. Note that the LBM of metals is generally followed by a stress-relieving heat treatment, but the simulation of this intermediate metallurgical step was not available in the version of the software used. However, the separation of the part from the building plate does not need to be simulated in our case, as the stress-relieving treatment is not accompanied by significant distortions while it avoids additional strains caused by the separation from the plate. Note that in the figures showing the simulation results, the building plate is hidden for better clarity, even though it is still present. A thermo-elastoplastic behavior is considered for the material response. The Prandtl-Reuss flow rule is considered for the plastic response using the Von Mises yield criterion and the uniaxial stress-strain curve. The required parameters for the simulations are thus the solidus temperature T_{sol}, chamber temperature T_{cham}, Young's modulus E, Poisson's ratio ν, coefficient of thermal expansion α, and the stress-strain curve in uniaxial tension of the material. For the sake of simplicity, material parameters are assumed to be independent of the temperature. As several simplification assumptions are considered for the finite element model, a correction of the results from experimental data was performed in post-processing (see Section 2.3).

Figure 1(a) shows an illustration of simulated thermal distortions for a ten-millimeter side cube made of Ti6Al4V titanium alloy (T_{sol} = 1868 K, E =, 113.8 GPa, ν = 0.342, α = 9.93e-6 K^{-1}, stress-strain curve in uniaxial tension given in Figure 2 (ESI Group, 2018)) with a chamber temperature T_{cham} equal to 293 K. The expected contour is indicated in red. Two faces of the cube are named "A" and "B", respectively referring to a side surface and the top surface of the cube. The upper part of the cube is not shown in order to see the distortions in the middle of the cube. The bottom layer of the cube is subjected to very small distortions because of the presence of the building plate (not visible in the image). It is worth noting that both positive and negative vertical distortions are created during the manufacturing of the cube: see the value range in the color scale. Indeed, two main distortion modes can be identified for a given layer: horizontal shrinkage and warping, as illustrated in Figure 1(b). Horizontal thermal contraction is accompanied by displacements in the perpendicular direction due to the presence of the immediately lower layer (similarly to differential bending in a composite material).

Insert here Figure 1: Illustration of the thermal distortions appearing during LBM manufacturing: (a) simulation result for a ten-millimeter-per-side cube made from Ti6Al4V. Only the lower half of the cube is shown, with surface distortions amplified by ten to better visualize the deformed geometry; (b) two distortion modes involved in a given layer

Insert here Figure 2: Stress-strain curve in uniaxial tension of the Ti6Al4V titanium alloy considered for the simulations (ESI Group, 2018). The response in the plastic zone is defined by the coordinates of the red crosses

Three options are proposed in terms of mesh choice, namely non-conforming mesh, uniform mesh, and uniform mesh with striped strategy: see Figure 3(a). Simulations were performed with the three approaches using the same parameters as in Figure 1(a). Results are presented in Figure 3(b) in terms of flatness defects for faces A and B (see below for additional information about flatness defect assessment and mesh convergence). It can be seen that the three types of mesh lead to nearly the same flatness values for face A, which is perpendicular to the building plate: about 0.007 mm. Concerning face B, which is parallel to the building plate, the striped strategy leads to a higher value than the other two types of mesh (0.003 mm to be compared to about 0.002 mm). In theory, the striped strategy is better suited to the actual manufacturing process because the latter involves the melting and solidification of linear vectors. However, the striped mesh is questionable with respect to finite element sizes. Indeed, the width of actual vectors is in general some tens of micrometers. Actual vectors cannot be modeled by finite elements for parts of centimeter or decimeter dimensions (unrealistically large number of elements and calculation time). The non-conforming meshing strategy is by far the fastest, allowing coarse elements in the massive zones and small elements at the boundaries. As an order of magnitude, the calculation time with a non-conforming mesh is ten times shorter than with a uniform mesh. As a conclusion, it was decided to use a non-conforming mesh for all the simulations in the study, with additional post-processing based on comparisons with experimental data (see Section 2.3).

Insert here Figure 3: Comparison between three mesh strategies: (a) schematic view of the finite element distribution in a square layer; b) comparison between the flatness defects obtained for faces A and B of the cube in Figure 1(a), as a function of the chosen mesh strategy

Information can be given about mesh convergence and calculation time. Still for the parameters of the cube in Figure 1(a) and using a non-conforming mesh, Figure 4(a) shows the distortions obtained for three different mesh refinements. Large discrepancies are observed when comparing 2,000 nodes and 11,000 nodes, especially at the four vertical edges of the cube. Differences are small when comparing 11,000 nodes and 233,000 nodes. Figure 4(b) shows the variation in calculation time and in maximum distortion as a function of the number of nodes. For all the calculations, the layer thickness and the lumping factor were set to 40 µm and "10 layers per superlayer" respectively. All simulations were run in Distributed Memory Parallel (DMP) mode on two cores. It can be seen that the calculation time is nearly proportional to the number of nodes. Using 11,000 nodes is a good compromise because, even if there is a slight difference in distortion compared to the use of 56,000 nodes, the calculation time is about 5 times shorter. It can be noted that such a compromise is unavoidable in an industrial context, especially for the shape optimization of large and complex parts. Finally, it is worth noting that the distortion of the top layer is very small compared to the maximum distortion in the cube: see Figure 4(a). This result is not in contradiction with Figure 1(a), which showed large distortions of the middle layer. Indeed, let us recall that a given layer is cumulatively distorted by the successive manufacturing of the layers above. The first layer being slightly deformed (because of the building plate), the maximum distortions are found to be in the central zone of the cube, and not at the top.

Insert here Figure 4: Convergence of the finite element model for the cube in Figure 1 using a non-conforming mesh: (a) distortions obtained for three different numbers of nodes, (b) maximum distortion in the cube and calculation time as a function of the number of nodes

2.2 Assessment of geometric errors

The geometric *errors* due to thermal distortions are assessed from simulation results based on the principles of ISO 1101 GPS standards (International Organization for Standardization, 2017). Let us recall that a geometrical *specification* is defined by a tolerance expressed in millimeters, denoted t in the following. For an element of a given type (plane, cylinder…), t is the maximum allowed distance between two elements of the same type such that the space in-between contains the specified element. The tolerance zone can be constrained in orientation or position with respect to a reference datum, contrary to the case of shape

specifications, such as flatness. The verification of the geometrical quality of a manufactured part aims to check if the evaluated elements are contained within their tolerance zone. In practice, finding a zone that is equal or smaller than the tolerance zone and that contains the measured element is enough to conclude that the latter meets the specification. In the case of *shape* defect control, there is risk of false-negative conclusion by overestimating the defect. Indeed, finding a zone containing the measured element does not mean that the found zone is optimal, since the tolerance zone is not constrained in either orientation or position. The question can be solved by searching for the smallest possible zone containing the measured element. Several methodologies can be proposed to define such a zone. Among these methodologies, the construction of a mean plane (for instance by least-square approximation) is particularly relevant when many data are available. Indeed, such a mean plane is *a priori* in a favorable location to enable the encompassment of the distorted surface. Thus, it is proposed in the present approach to use the same methodology for the assessment of a shape defect value from the results of finite element simulation (providing data at each surface node of the mesh).

Figure 5 explains how flatness, parallelism and perpendicularity defects were calculated from the node clouds provided by the finite element model. For example, the flatness defect is defined by the minimum distance between two planes encompassing the point cloud parallel to the *mean plane* (see Figure 5(a)). In the present study based on finite element simulations, the surface element is defined by the mesh nodes in the distorted configuration. The *mean plane* is defined by mean-square approximation. The same approach can be carried out for orientation defects, such as the parallelism and perpendicularity defects in Figures 5(b) and (c) respectively.

Insert here Figure 5: Assessment of geometric defects from simulation results: a) flatness defect; (b) parallelism defect, (c) perpendicularity defect. Point clouds correspond to the final locations of the nodes of the finite element model, *i.e.* in deformed configuration

Figure 6 provides an example of the flatness defect assessment for a 30×30×30 mm^3 cube. Figure 6(b) shows the point cloud corresponding to the face located at y = -15 mm in the CAD model. As expected, the bottom and top layers are slightly distorted (see Section 2.1): y ≈ -14.85 mm in the deformed configuration. It can be noted in Figure 6(c) that the distribution of horizontal shrinkage is not symmetrical, leading to a mean plane which is slightly inclined

with respect to the vertical direction. The flatness defect is indicated in Figure 6(c); however the value must be corrected to take into account errors in the model, as explained in the next section.

Insert here Figure 6: Example of the flatness defect assessment for a 30×30×30 mm cube: (a) illustration of the expected and obtained geometry, (b) point cloud corresponding to the distorted vertical left-hand face, (c) identification of the corresponding flatness defect

2.3 Comparison with experimental data

A comparison with experimental data was performed to correct potential errors in the simulated data caused by the simplification hypotheses of the finite element model. Figure 7(a) shows two parts made from Ti6Al4V titanium alloy. They were produced by the AddUp company, Cébazat, France. They remained attached to the building plate during the geometric analysis, which was performed using a coordinate measuring machine (CMM). They exhibit a specific shape prone to significant flatness defects on the vertical surfaces. This geometry is inspired by a real industrial case developed by AddUp. Part 1 was designed first and modeled using the software presented in Section 2.1, confirming the presence of a large flatness defect on the vertical surfaces. Part 2 was designed after a procedure designed to reduce the flatness defect (see Section 3.2 for more about this procedure). Flatness defects were experimentally measured on four faces: faces F_1 and F_2 belonging to part 1, and faces F_3 and F_4 belonging to part 2; see Figure 7(b). Figure 8 presents the simulated flatness defects as a function of the experimental flatness defects. The following comments can be made from these graphs:

- a preliminary statistical analysis of measurement errors showed that the resolution in the touch probe location is equal to ±0.03 mm. Equivalent uncertainty bars have been indicated in the graphs for the experimental flatness defects;
- a perfect agreement between simulated and experimental results would have corresponded to points located on the bisector of the graph (black solid line). A large discrepancy can be observed between experimental and numerical data: see red points. However, points are globally aligned along a straight line (dashed line). This means that the higher the simulated flatness defect, the higher the experimental flatness defect, in a proportional fashion;
- the linear discrepancy between simulated and experimental data is difficult to

interpret. Indeed, distortions associated with LBM manufacturing are not intuitive because of the specific deformation mode (successive creation of layers, cumulative distortions of the already solidified layer, first and last layers slightly deformed), and more generally because of the multi-scale and multi-physics character of the process. However, the linear discrepancy could be partially explained by a Young's modulus (E) and a coefficient of thermal expansion (α) considered as constant in the simulations, which is a strong hypothesis. Actually E increases and α decreases during cooling from solidus temperature to chamber temperature, and there are also potential dilatometric anomalies due to solid-solid phase transformations. Other explanations can be proposed: the complex behavior of the "interface" between the created layer and the already solidified layers (re-melted zone), or the temperature gradient in the already solidified layers;

- we propose to modify the simulated flatness defects by applying a correction coefficient. The identified multiplication coefficient is equal to 0.172. It is expected that the multiplication coefficient depends on the powder specifications as well as on the manufacturing strategy. Corrected data are also plotted in Figure 8: see blue points, close to the bisector. It must be noted that a similar approach is difficult to apply to the top (horizontal) layers. Indeed, by construction, the top layers are only slightly distorted. Experimental measurements have shown that the roughness defect is of the same order of magnitude as the horizontal flatness defect (parts produced by AM are known to have poor surface roughness). It was decided to apply the same correction coefficient to the simulated flatness defects of the horizontal surfaces.

Insert here Figure 7: Experimental assessment of flatness defects for comparison purposes with simulated results: (a) two parts made from Ti6Al4V alloy attached to the building plate and placed in a coordinate measuring machine; (b) four surfaces considered for flatness defect measurement

Insert here Figure 8: Comparison between simulated and experimental flatness defects for the two parts in Figure 7. In red: raw data. The dashed line features a linear trend between numerical and experimental data. In blue: after correction of the numerical data. The solid line corresponds to the bisector, for which numerical and experimental data are equal

3. Applications to two types of geometrical features

An advantage offered by numerical simulation is that of reducing the amount of experimental and empirical study required during machine set-up. The idea of using simulation is not to entirely replace the design of experiments (DoE), but to give some tools to the operator to quickly focus on a functional zone in the whole parameter space. Simulation also enables the user to gain experience and knowledge. For illustration purposes, Sections 3.1 and 3.2 provide results for a simple and a complex geometry respectively.

3.1 Walls

A simple geometric case was first studied: a wall. Walls are an elementary design block commonly found in AM. Suspended zones of a printed part are also often supported by thin removable walls. Figure 9(a) presents the square-wall geometry that is considered in the study, involving three flatness specifications (tolerance values $t1$, $t2$ and $t3$, not quantitively defined here). The wall is defined by two dimensions: a and b, with $a \geq b$ and a varying from 5 mm to 50 mm. Figures 9(b), (c) and (d) show the influence of these dimensions on the flatness defect of faces A, B and C respectively. In the three cases within the range of parameters tested, the larger the surface $a \times b$, the greater the flatness defect. More precisely, the trend appears to be linear along both the a-axis and b-axis for vertical faces:

$$\text{flatness defect of face A} = 6.84\ 10^{-4}\ a + 2.94\ 10^{-4}\ b \quad (1)$$

$$\text{flatness defect of face C} = 2.47\ 10^{-4}\ a + 7.31\ 10^{-4}\ b \quad (2)$$

In both cases, the R-squared coefficient associated with the linear regression is greater than 0.97. For $a = b$ (cubic geometry), flatness defects on faces A and C are logically equal due to symmetry. For horizontal surface B, the order of magnitude of the flatness defect is more than 10 times smaller than for faces A and C, even for the maximum size tested (a cube of 50 mm per side). The zoom in Figure 9(c) shows that the variation in the flatness defect with a and b is not linear, especially for small values for parameter b (lower than 5 mm).

Before presenting a more complex case in the next section, Figures 10(a) and (b) show an

extension of the present approach to the assessment of parallelism and perpendicularity defects, without correction, unlike flatness data. It is interesting to note the strong non-linearity in the perpendicularity defect, in particular for a cubic configuration: see Figure 10(b) for $a = b$. Even if the wall geometry is simple, such numerical results provide general trends which can be useful for designers in addition to DoE.

Insert here Figure 9: Application to a wall: (a) geometry and flatness specifications, (b) (c) (d) flatness defects obtained by numerical approach as a function of dimensions *a* and *b*, for faces A, B and C respectively. Simulations were performed for a Ti6Al4V alloy

Insert here Figure 10: Application to parallelism and perpendicularity: (a) specifications, (b) (c) parallelism and perpendicularity defects obtained by simulation as a function of dimensions *a* and *b* of the wall

3.2 Complex geometry

A more complex shape is now considered. Figure 11(a) shows the CAD model of Part 1 in Figure 7. The geometry and dimensions of the part are inherited from an industrial case. Face F of this part features a simulated defect flatness of 0.241 mm. Note that all the simulated defects presented in this section have been corrected with the previously determined factor (see Section 2.3). Reducing flatness defects for this type of complex shape is not intuitive, and performing a complete DoE would be long and costly. The aim of the present section is to show that it is possible to improve the geometric quality from simulations. Note that the objective here is not to carry out a full optimization procedure (see the conclusion section for the perspectives of the study); the objective is to quickly determine which element of this complex geometry has the greatest influence on the flatness defect of face F. Only four geometrical parameters were allowed to change, while keeping the others constant: see p_1, p_2, p_3 and p_4 in Figure 11(b). From the reference simulation (#1 in Table 1), each parameter was increased or decreased, keeping the other parameters as in the reference simulation. Table 1 gives the values for the flatness defects of face F obtained by simulation. It is interesting to note that increasing or decreasing parameter p_1 has the same effect: a diminution of the flatness defect (compare #2 and #3 with reference simulation #1). The same is true for parameter p_4 (see #8 and #9). On the contrary, opposite effects are observed when modifying

parameters p_2 and p_3: the flatness defect can increase or decrease as a function of the direction of variation of the input parameter. In particular, a strong reduction is obtained for simulation #5, corresponding to a flatness defect decreased by 58% with respect to simulation #1. For these two configurations (#1 and #5), Figure 12(a) shows the distributions of distortion along the *x*-axis, *i.e.* perpendicularly to face F, with respect to the CAD model. Main differences are observed in the circled zones in the figure. Figures 12(b) and (c) present the node clouds of the zone featuring the largest distortions, for simulations #1 and #5 respectively. The mean plane of the node cloud (defined over the whole surface F) is also shown for both cases. An improvement in geometrical quality is clearly observed when comparing the zoomed zones. Experimental validation was performed by manufacturing the reference configuration #1 and the improved configuration #5. Measurements were provided in Section 2.3 (Figure 8), confirming the reduction in the flatness defect: from 0.239 mm for #1 to 0.118 mm for #5. Finally, Figure 13(a) shows the residual Von Mises stresses for simulations #1 and #5 respectively. Values are clearly greater in the improved part than in the reference one. The plasticized zones are visible in Figure 13(b), in which the color scale was modified compared to Figure 13(a): grey color corresponds to Von Mises stresses greater than the elastic limit (900 MPa, see Figure 2). The part corresponding to improved configuration #5 clearly undergoes more plasticization than the part corresponding to reference configuration #1. It is interesting to note that geometrical distortions and residual stresses varied in opposite directions: a decrease in geometrical distortions was accompanied by an increase in residual stresses.

Insert here Figure 11: Application to a complex geometry likely to exhibit a strong flatness defect: (a) CAD view of part 1 in Figure 7, (b) side view with four parameters allowed to change in order to reduce the flatness defect associated with face F

Insert here Table 1: Flatness defects of face F in Figure 11(b) obtained by simulation for different values of dimensional parameters p_1, p_2, p_3 and p_4

Insert here Figure 12: Improvement of the geometric quality of face F in Figure 11, from simulations: (a) distortions perpendicular to face F with respect to the CAD model, (b) (c) node cloud of face F in distorted configuration and associated mean plane, for the reference part (#1) and the improved part (#5) respectively

Insert here Figure 13: (a) Residual Von Mises stress fields, (b) same with suitable color scale to highlight plasticized zones. Von Mises stresses greater than the elastic limit are in grey color

4. Conclusion

A numerical approach inspired by GPS standards was developed in this study for the assessment of thermal distortions occurring during LBM additive manufacturing. The work pointed out how complex the question of the simulation of these geometrical distortions is. Thanks to finite element software provided by ESI Group, we were able to highlight that fast simulations of macroscopic distortions can be carryed out to provide the designer with design rules. Despite the intrinsically multi-scale and multi-physics character of the LBM process, the macroscopic simulations correctly captured variations in the flatness defect as a function of the geometric parameters. The main advantage of using an approach based on GPS standards is that it does not require a comparison between expected (CAD model) and obtained surfaces for geometrical defect assessment, which avoids the question of their positioning in relation to each other, both in simulations and for real measurements on manufactured parts. The method is applicable from the design phase. The methodology enables the assessment of the process capability of printing a given part/assembly, and the improvement of its design prior to the manufacturing stage. Finally, the present study is a first step towards full optimization, complementary/preliminary to design of experiments. Figure 14 proposes that geometrical specifications could be used as requirements for parametric optimization or even topological optimization, involving the residual stress field as a cost function. The prospects in terms of shape optimization will allow us to take better advantage of the new possibilities offered by the LBM additive manufacturing process.

Insert here Figure 14: Optimization based on geometrical specifications

References

Becker, T.H. and Dimitrov, D. (2016), "The achievable mechanical properties of SLM produced Maraging Steel 300 components", *Rapid Prototyping Journal*, Vol. 22 No. 3, pp.487-494. https://doi.org/10.1108/RPJ-08-2014-0096

Braian, M., Jimbo, R. and Wennerberg, A. (2016), "Production tolerance of additive manufactured polymeric objects for clinical applications", *Dental Materials*, Vol. 32 No. 7, pp. 853-861. http://doi.org/10.1016/j.dental.2016.03.020

Dantan, J. Y., Huang, Z., Goka, E., Homri, L., Etienne, A., Bonnet, N. and Rivette, M. (2017), "Geometrical variations management for additive manufactured product", *CIRP Annals - Manufacturing Technology*, Vol. 66 No. 1, pp 161-164. http://doi.org/10.1016/j.cirp.2017.04.034

Douellou, C., Balandraud X. and Duc, E. (2019) "Fatigue characterization of 3D-printed maraging steel by infrared thermography". in Kramer S., Jordan, J., Jin, H., Carroll, J. and Beese, A. (Eds), *Mechanics of Additive and Advanced Manufacturing, Volume 8. Conference Proceedings of the Society for Experimental Mechanics Series, June 4-7, 2018 in Greenville, SC, USA*, Springer, Cham, pp. 5-9. https://doi.org/10.1007/978-3-319-95083-9_2

ESI Group (2018), ESI Additive Manufacturing 2018.0, available at https://www.esi-group.com/software-solutions/virtual-manufacturing/additive-manufacturing/esi-additive-manufacturing

Hällgren, S., Pejryd, L. and Ekengren, J. (2016), "3D Data Export for Additive Manufacturing-Improving Geometric Accuracy", *Procedia CIRP*, Vol. 50, pp. 518-523. http://doi.org/10.1016/j.procir.2016.05.046

Huang, Z., Dantan, J.Y., Etienne, A., Rivette, M. and Bonnet, N. (2018). "Geometrical deviation identification and prediction method for additive manufacturing", *Rapid Prototyping Journal*, Vol. 24 No. 9, pp. 1524-1538. https://doi.org/10.1108/RPJ-07-2017-0137

International Organization for Standardization (2017), "ISO 1101: Geometrical Product Specifications (GPS) – Tolerances of form, orientation, location and run out", 2017-04-01.

Jared, B.H., Aguilo, M.A., Beghini, L.L., Boyce, B.L., Clark, B.W., Cook, A., Kaehr, B.J. and Robbins, J. (2017), "Additive manufacturing: Toward holistic design", *Scripta Materialia*, Vol. 135, pp. 141-147. http://doi.org/10.1016/j.scriptamat.2017.02.029

Jin, Y., He, Y., Fu, G., Zhang, A. and Du, J. (2017), "A non-retraction path planning approach for extrusion-based additive manufacturing", *Robotics and Computer-Integrated Manufacturing*, Vol. 48, pp. 132-144. http://doi.org/10.1016/j.rcim.2017.03.008

Lieneke, T., Adam, G.A.O., Leuders, S., Knoop, F., Josupeit, S., Delfs, P., Fuke, N. and Zimmer, D. (2015), "Systematical determination of tolerances for additive manufacturing by measuring linear dimensions", in Bourell, D.L. (Ed.) *Proceedings: 26th Annual International Solid Freeform Fabrication Symposium - an Additive Manufacturing Conference, August 10-12, Austin, Texas, USA*, University of Texas at Austin, pp. 371-384.

Lieneke, T., Denzer, V., Adam, G.A.O. and Zimmer, D. (2016), "Dimensional Tolerances for Additive Manufacturing: Experimental Investigation for Fused Deposition Modeling", *Procedia CIRP*, Vol. 43, pp. 286-291. http://doi.org/10.1016/j.procir.2016.02.361

Mahshid, R., Mansourvar, Z. and Hansen, H.N. (2017), "Tolerance analysis in manufacturing using process capability ratio with measurement uncertainty", *Precision Engineering*, Vol. 52, pp. 201-210. http://doi.org/10.1016/j.precisioneng.2017.12.008

Megahed, M., Mindt, H.W., N'Dri, N. Duan, H.Z. and Desmaison, O. (2016), "Metal additive-manufacturing process and residual stress modeling", *Integrating Materials and Manufacturing Innovation*, Vol. 5, article number 4. https://doi.org/10.1186/s40192-016-0047-2

Moroni, G., Petrò, S. and Polini, W. (2017), "Geometrical product specification and verification in additive manufacturing", *CIRP Annals - Manufacturing Technology*, Vol. 66 No. 1, pp. 157-160. http://doi.org/10.1016/j.cirp.2017.04.043

Peng, H., Ghasri-Khouzani, M., Gong, S., Attardo, R., Ostiguy, P., Gatrell, B.A., Budzinski, J., Tomonto, C., Neidig, J., Shankar, M.R., Billo, R., Go, D.B. and Hoelzle, D. (2018), "Fast prediction of thermal distortion in metal powder bed fusion additive manufacturing: Part 1, a thermal circuit network model", *Additive Manufacturing*, Vol. 22, pp. 852-868. https://doi.org/10.1016/j.addma.2018.05.023

Peng, H., Ghasri-Khouzani, M., Gong, S., Attardo, R., Ostiguy, P., Gatrell, B.A., Budzinski, J., Tomonto, C., Neidig, J., Shankar, M.R., Billo, R., Go, D.B. and Hoelzle, D. (2018), "Fast prediction of thermal distortion in metal powder bed fusion additive manufacturing: Part 2, a quasi-static thermo-mechanical model", *Additive Manufacturing*, Vol. 22, pp. 869-882. https://doi.org/10.1016/j.addma.2018.05.001

Ponche, R., Kerbrat, O., Mognol, P. and Hascoet, J.Y. (2014), "A novel methodology of design for Additive Manufacturing applied to Additive Laser Manufacturing process", *Robotics and Computer-Integrated Manufacturing*, Vol. 30 No. 4, pp. 389-398.

http://doi.org/10.1016/j.rcim.2013.12.001

Santos, L.M.S., Ferreira, J.A.M., Jesus, J.S., Costa, J.M., Capela, C. (2016), "Fatigue behaviour of selective laser melting steel components", *Theoretical and Applied Fracture Mechanics*, Vol. 85, pp. 9-15. https://doi.org/10.1016/j.tafmec.2016.08.011

Shahrain, M., Didier, T., Lim, G. K. and Qureshi, A.J. (2016), "Fast Deviation Simulation for “Fused Deposition Modeling” Process", *Procedia CIRP*, Vol. 43, pp. 327-332. http://doi.org/10.1016/j.procir.2016.02.004

Sossou, G., Demoly, F., Montavon, G., & Gomes, S. (2017), "An additive manufacturing oriented design approach to mechanical assemblies", *Journal of Computational Design and Engineering*, Vol. 5 No. 1, pp. 3-18. http://doi.org/10.1016/j.jcde.2017.11.005

Umaras, E. and Tsuzuki, M.S.G. (2017), "Additive Manufacturing - Considerations on Geometric Accuracy and Factors of Influence", *IFAC-PapersOnLine*, Vol. 50 No. 1, pp 14940-14945. http://doi.org/10.1016/j.ifacol.2017.08.2545

Yap, Y.L., Wang, C., Sing, S.L., Dikshit, V., Yeong, W.Y. and Wei, J. (2017), "Material jetting additive manufacturing: An experimental study using designed metrological benchmarks", *Precision Engineering*, Vol. 50, pp 275-285. http://doi.org/10.1016/j.precisioneng.2017.05.015

Zhu, Z., Anwer, N. and Mathieu, L. (2017), "Deviation Modeling and Shape Transformation in Design for Additive Manufacturing", *Procedia CIRP*, Vol. 60, pp. 211–216. http://doi.org/10.1016/j.procir.2017.01.023

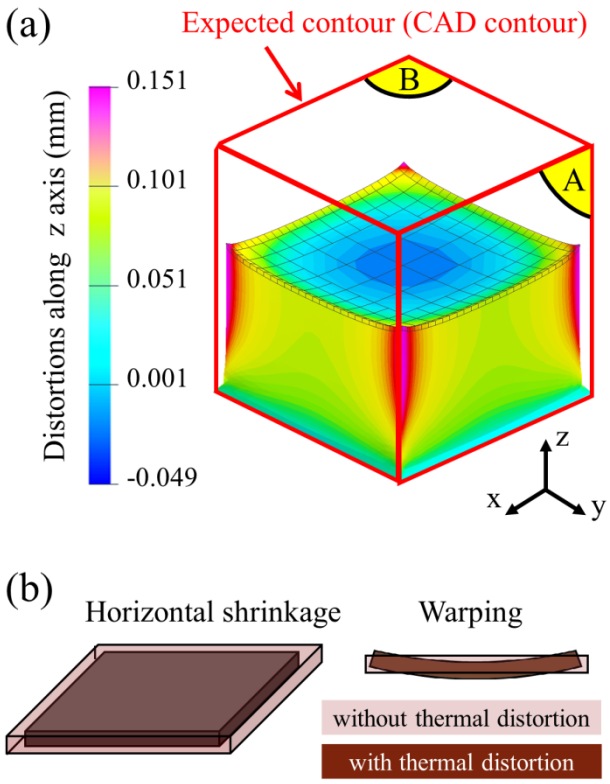

Figure 1 Illustration of the thermal distortions appearing during LBM manufacturing: (a) simulation result for a ten-millimeter-per-side cube made from Ti6Al4V. Only the lower half of the cube is shown, with surface distortions amplified by ten to better visualize the deformed geometry; (b) two distortion modes involved in a given layer

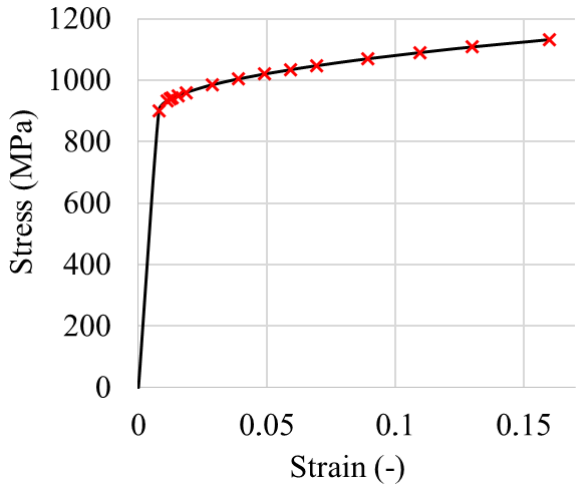

Figure 2 Stress-strain curve in uniaxial tension of the Ti6Al4V titanium alloy considered for the simulations (ESI Group, 2018). The response in the plastic zone is defined by the coordinates of the red crosses

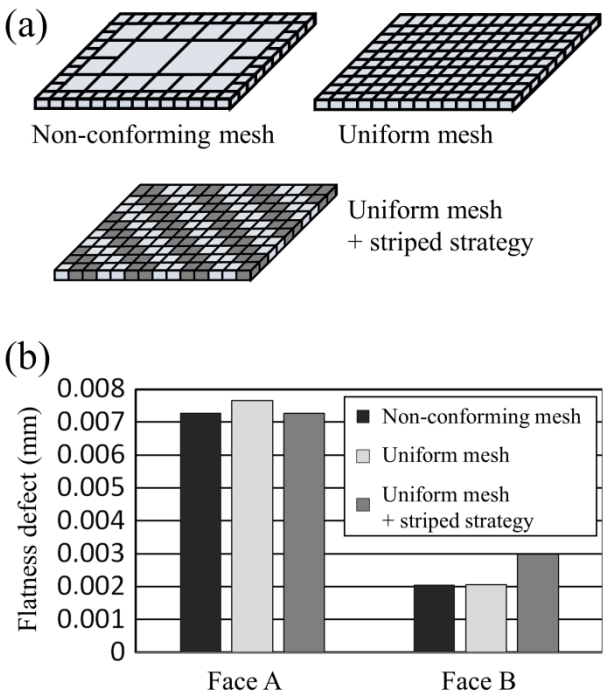

Figure 3 Comparison between three mesh strategies: (a) schematic view of the finite element distribution in a square layer; b) comparison between the flatness defects obtained for faces A and B of the cube in Figure 1(a), as a function of the chosen mesh strategy

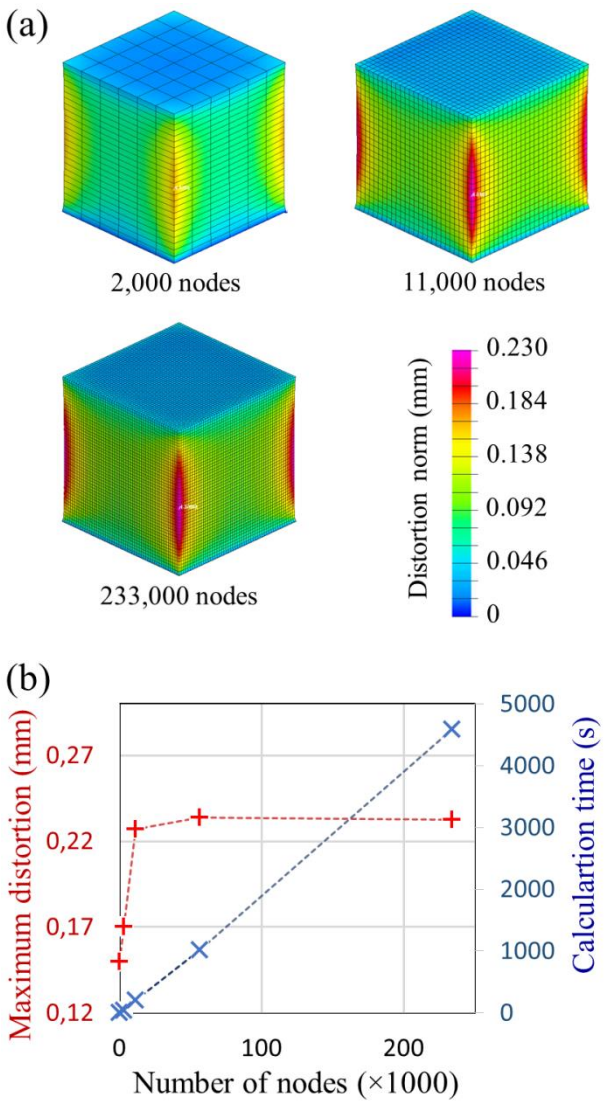

Figure 4 Convergence of the finite element model for the cube in Figure 1 using a non-conforming mesh: (a) distortions obtained for three different numbers of nodes, (b) maximum distortion in the cube and calculation time as a function of the number of nodes

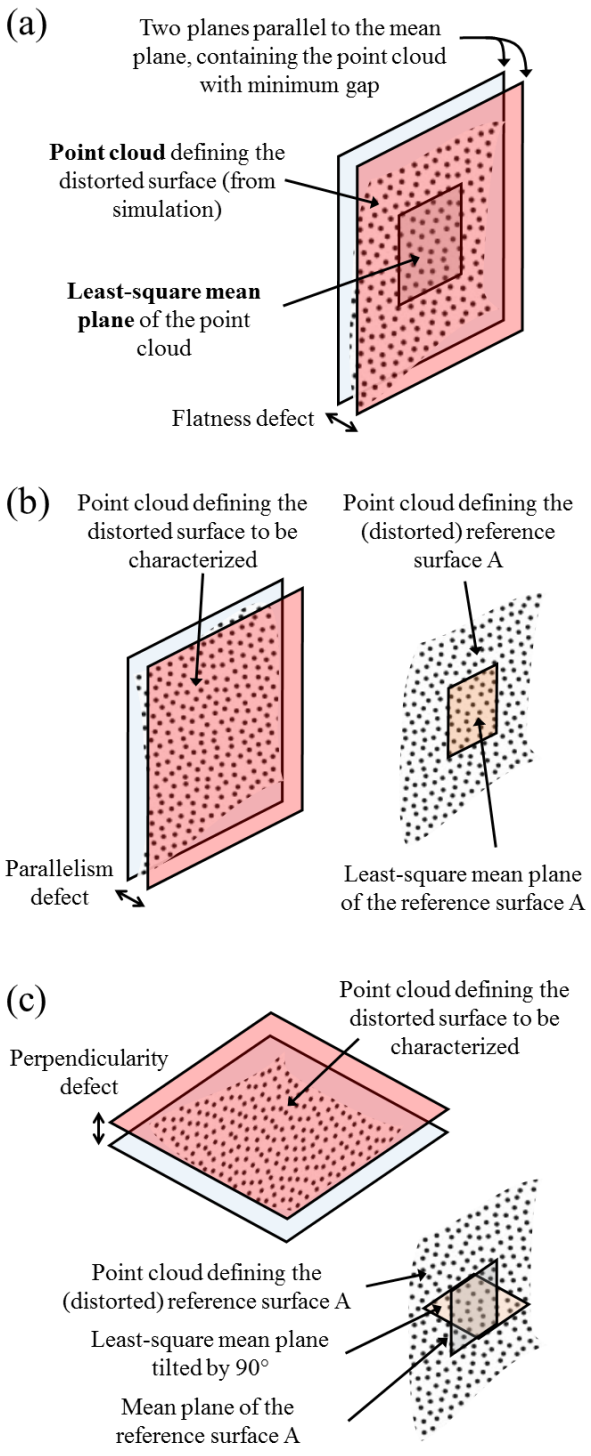

Figure 5 Assessment of geometric defects from simulation results: a) flatness defect, (b) parallelism defect, (c) perpendicularity defect. Point clouds correspond to the final locations of the nodes of the finite element model, *i.e.* in deformed configuration

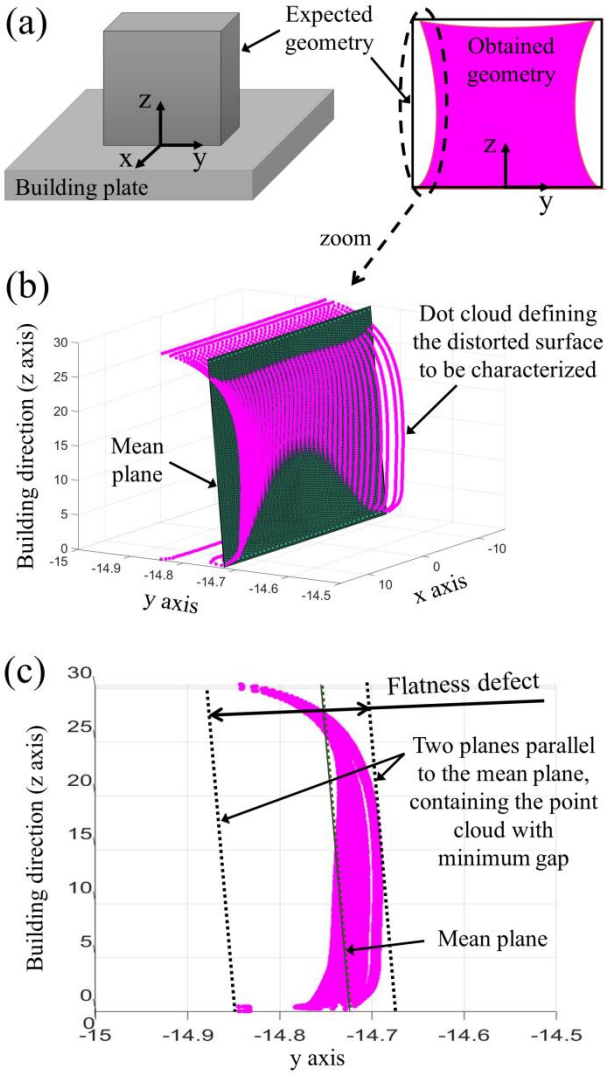

Figure 6 Example of the flatness defect assessment for a 30×30×30 mm cube: (a) illustration of the expected and obtained geometry, (b) point cloud corresponding to the distorted vertical left-hand face, (c) identification of the corresponding flatness defect

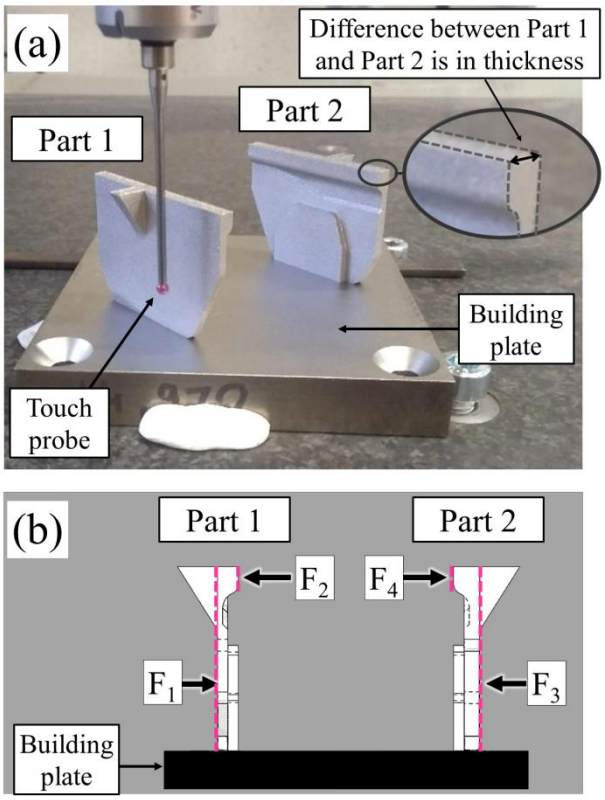

Figure 7 Experimental assessment of flatness defects for comparison purposes with simulated results: (a) two parts made from Ti6Al4V alloy attached to the building plate and placed in a coordinate measuring machine; (b) four surfaces considered for flatness defect measurement

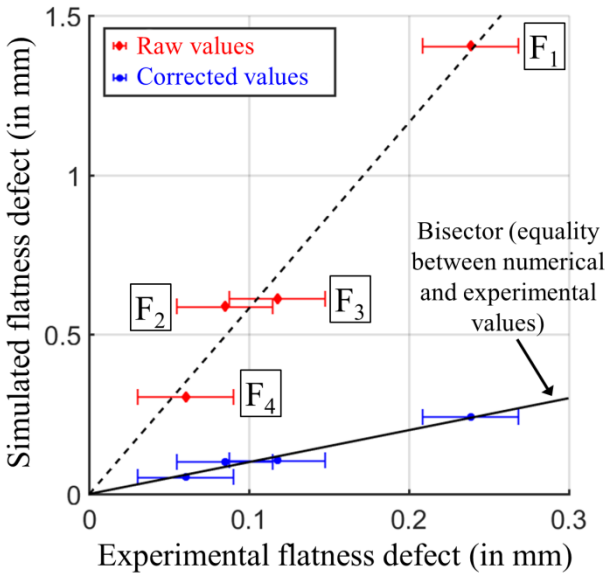

Figure 8 Comparison between simulated and experimental flatness defects for the two parts in Figure 7. In red: raw data. The dashed line features a linear trend between numerical and experimental data. In blue: after correction of the numerical data. The solid line corresponds to the bisector, for which numerical and experimental data are equal

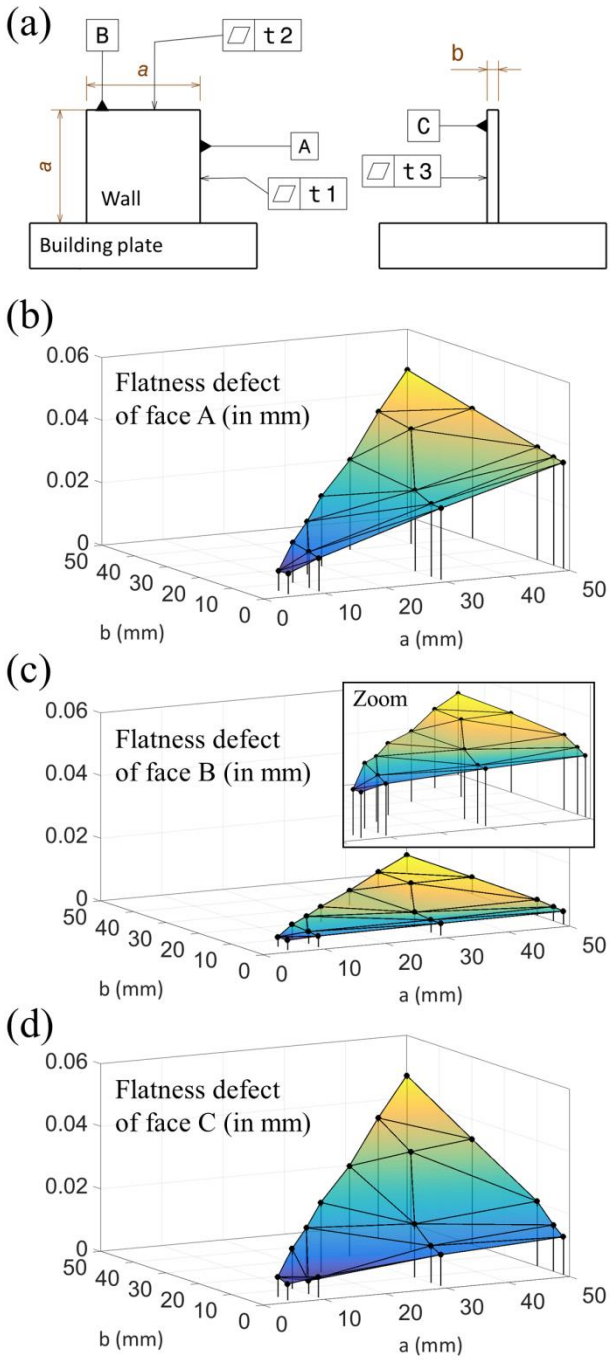

Figure 9 Application to a wall: (a) geometry and flatness specifications, (b) (c) (d) flatness defects obtained by numerical approach as a function of dimensions *a* and *b*, for faces A, B and C respectively. Simulations were performed for a Ti6Al4V alloy

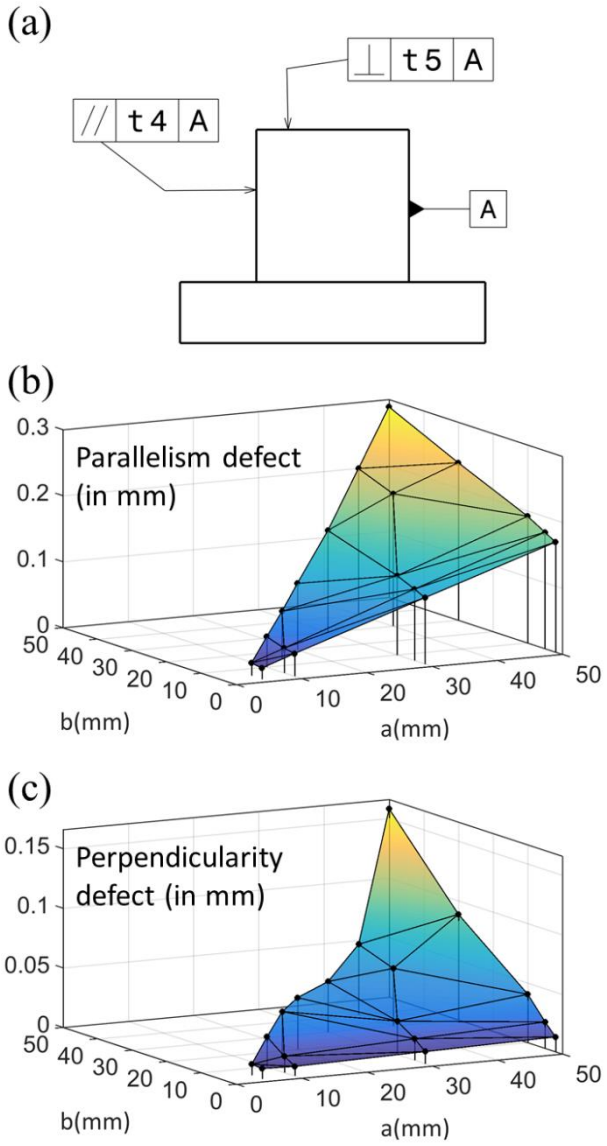

Figure 10 Application to parallelism and perpendicularity: (a) specifications, (b) (c) parallelism and perpendicularity defects obtained by simulation as a function of dimensions *a* and *b* of the wall

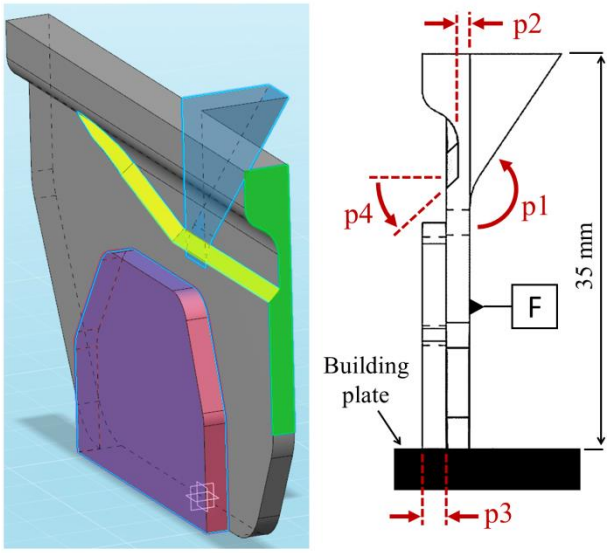

Figure 11 Application to a complex geometry likely to exhibit a strong flatness defect: (a) CAD view of part 1 in Figure 7, (b) side view with four parameters allowed to change in order to reduce the flatness defect associated with face F

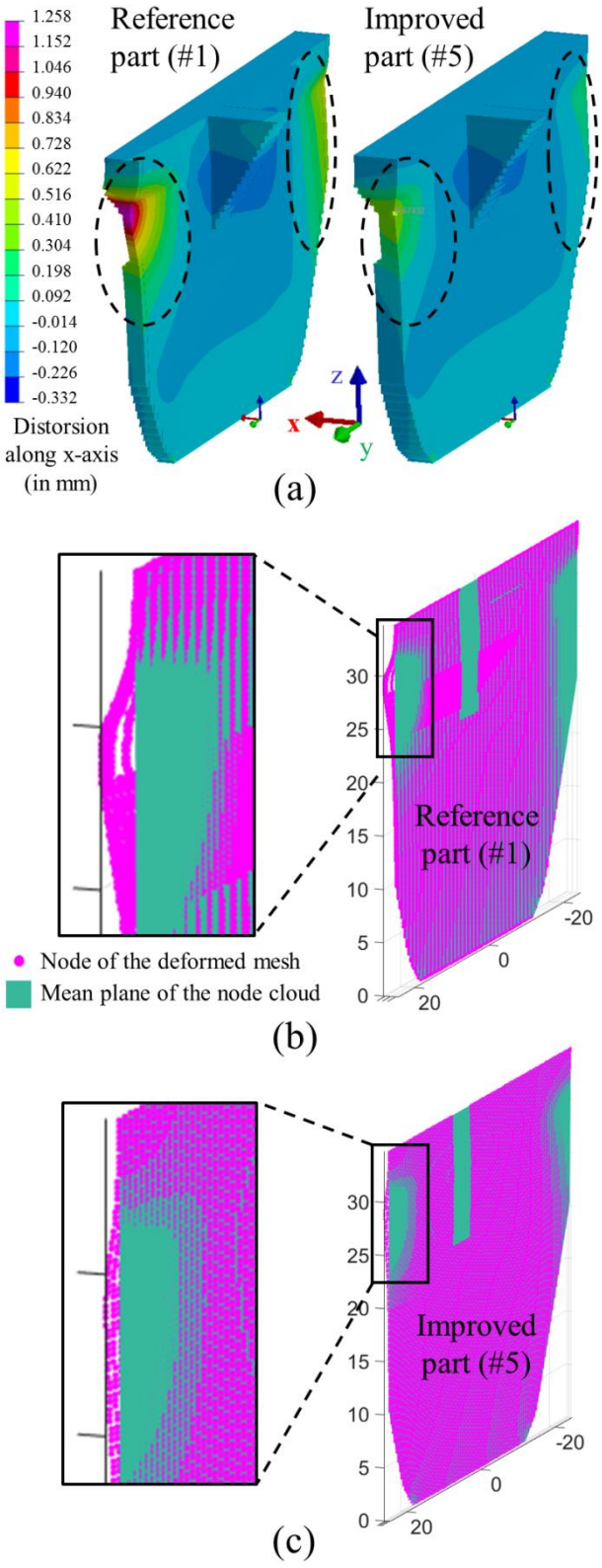

Figure 12 Improvement of the geometric quality of face F in Figure 11, from simulations: (a) distortions perpendicular to face F with respect to the CAD model, (b) (c) node cloud of face F in distorted configuration and associated mean plane, for the reference part (#1) and the improved part (#5) respectively

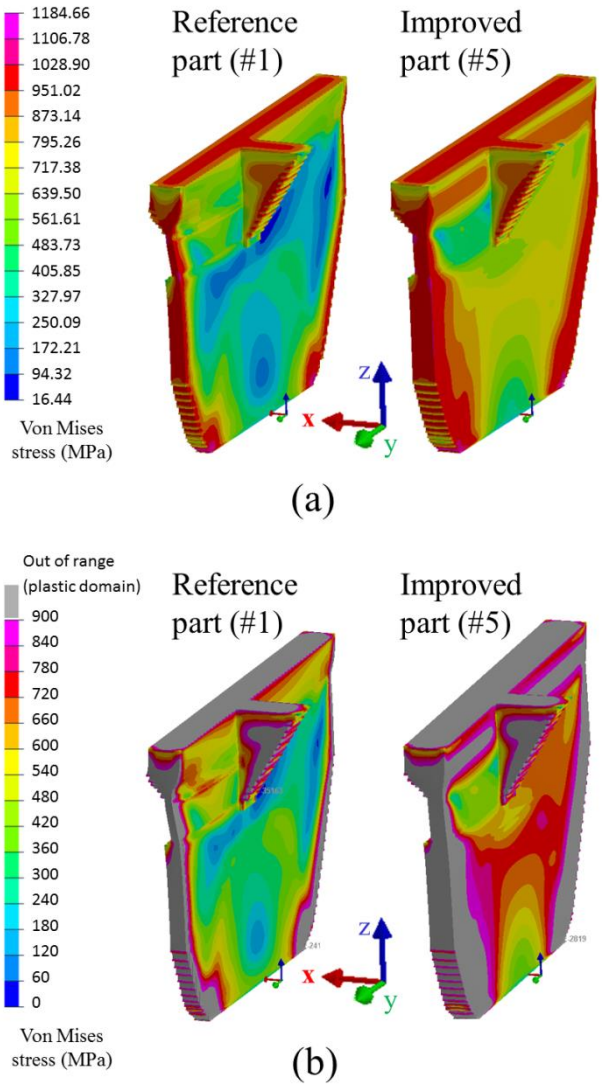

Figure 13 (a) Residual Von Mises stress fields, (b) same with suitable color scale to highlight plasticized zones. Von Mises stresses greater than the elastic limit are in grey color

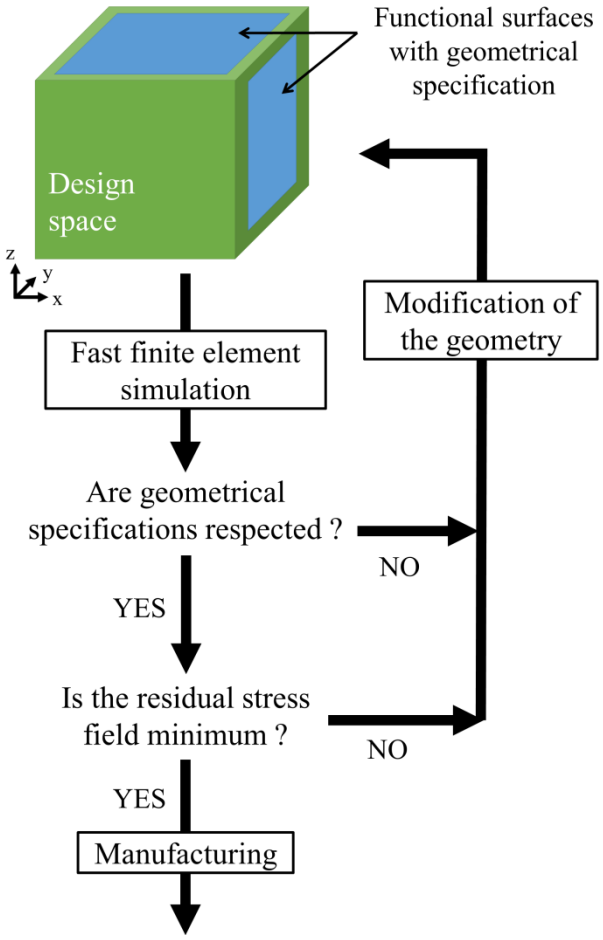

Figure 14 Optimization based on geometrical specifications